Article

Hyperconcentrated flows shape bedrock channels

Check for updates

Verena Stammberger ✉, Benjamin Jacobs & Michael Krautblatter

Geomorphological evidence of incised bedrock channels is widespread in all mountain landscapes worldwide. However, the processes controlling incision and gorge formation in bedrock have not directly been observed in an actualistic way. Here, we show a LiDAR change detection deciphering the erosive power of a 60,000 m^3 hyperconcentrated flow (transition between flood and debris flow) in a deeply incised rock gorge in June, 2020. The flow laterally eroded up to 1 m of massive limestone and widened a 4 m narrow section of the gorge by up to 15%. Sinuosity, convergence, and gradient of the channel were proven to not influence erosivity indicating the hyperconcentrated nature of erosion. Furthermore, other than in prior studies no abrasion of thin rock veneer dominates erosion but mechanically excited breakout of rock fragments. Magnitude-frequency relations of eroded volumes mimic subaerial rock wall retreat. We show how single hyperconcentrated flows can erode bedrock channels far more efficient than decades of turbulent flows and hypothesise that repeated hyperconcentrated flows in phases of enhanced precipitation or by elevated material supply could control erosion boosts in gorge formation, e.g. in the Lateglacial or during climatic fluctuations.

Spectacular canyons on earth are assumed to be incised over millions of years by moderate flows[1,2], others are assumed to have formed rapidly during extreme flood events[3–8], as a consequence of relief rejuvenation due to a base-level drop[9–12] or to be scoured through subglacial meltwater[13,14]. The question of how and consequently in which period of time inner gorges in the Central Alps were formed raises a controversial discussion in the scientific community. This discussion reaches long back[15] with a description of hillslope convexity adjacent to down-cutting channels producing an inner gorge[9]. Since then, varying explanations on the genesis of inner gorges have been provided. Due to the elevated sediment yield during deglaciation[16] and post-glacial fluvial systems[17,18] many studies assume the rapid fluvial erosion after the Last Glacial Maximum[19–23] while others support the alternative theory of a successive genesis during glacial-interglacial cylces[24–26]. The Last Glacial Maximum theory is supported by the concept that glacial erosion rates surpass fluvial incision[27] and therefore eradicate gorges during glacial periods.

To get closer to answering this question, one needs to understand the erosive processes acting in bedrock channels and the proportional contributions of erosion by single extreme events compared to steady fluvial incision. Numerous studies could demonstrate erosion and entrainment by debris flows in loose sediment[28–31] as well as in laboratory experiments[32,33]. Yet, only a handful of directly observed bedrock erosion events during extreme discharges exist[5,12,34–36] and observations contribute substantially to the understanding of the controlling mechanisms.

Erosive processes in sediment- as well as bedrock-channels are well studied for turbulent flows. Entrainment in loose sediment beds occurs either when basal shear forces of the flow mobilise the bed sediment[37,38] or due to normal stresses by particle collisions. Latter process is also hypothesised to be a major driver of bedrock erosion[39] varying with the fracture spacing[40] and the orientation of faults and joints[7,41]. Several single mechanisms control the rate of bedrock incision in turbulent flows including abrasion by bed- and suspended load, plucking, cavitation, dissolution, fracturing and loosening of joint blocks as well as the sediment coverage of the bedrock channel[42–54]. The erosion pattern during turbulent flows is governed by a number of effects e.g., refs. [48,50,53], of which two are assumed to be most important: The tools effect describes how an increasing amount of moving bedload particles leads to more impacts on the bedrock and therefore a higher erosion e.g., refs. [42,55,56]. But if the sediment supply exceeds the transport capacity, the cover effect prevents the bedrock from being impacted by the bedload and therefore decreases the vertical erosion e.g., refs. [52,57,58]. The highest bedrock erosion rates in fluvial regimes seem to occur at a moderate bedload relative to the transport capacity depending on the cover effect (sediment cover shielding the bed from abrasion and plucking) as well as the saltating grain size[48,50]. Therefore, the sediment

Chair of Landslide Research, TUM School of Engineering and Design, Technical University of Munich, Arcisstraße 21, Munich 80333 Bavaria, Germany.
✉e-mail: verena.stammberger@tum.de

predisposition as well as the distribution and mobilisation during the flow has a major impact on the rates and locations of vertical bedrock erosion.

Another factor is the channel geometry: by forming alluvial point bars on the inner banks and directing the flow towards the outer banks, bedrock erosion is enhanced at the latter[59] and therefore showing a clear dependence on the sinuosity of channels[60,61]. Together with the slope and the confinement of the channel, this sinuosity is also an important key control of lateral migration and therefore channel bank erosion in turbulent flows[62,63]. For meandering rivers, the bank geometry[64,65], the curvature of the channel above the bend as well as the geometry of the bend[66,67] influence the rate of lateral migration. The smaller the channel radius of a bend, the higher the magnitude of the centrifugal force[68-71] directing the flow towards the outer channel bank and consequently increasing the bank erosion rate. If secondary flow cells (lateral, not in the direction of the general flow) are dominant, the bank erosion at the bend apex is limited due to the protecting behaviour of the cells[72]. Enhanced migration in bends of meandering streams not only occur in loose sediment channels but also in fluvial bedrock channels[61] and solutional channels in limestone caves[60]. Regarding the slope, experimental studies showed increased bedload abrasion with increasing channel slope[73,74]. Further erosion patterns in bedrock are shown in ref. [36], where the highest erosion rates were measured close to the bed as well as on obstacles protruding the flow. The lateral erosion in turbulent flows is highly pronounced close to the bed (and therefore the bedload) and rapidly decreases with increasing elevation from the bed[36,52,59].

Looking at a larger timescale, empirical models for catchment or channel evolution are either coupling the stream power[46,75-80] or boundary shear stress[81,82] to fluvial incision of channel networks in catchments with various characteristics. Because most of these models do not directly factor in the physical processes of channel erosion, many studies conclude that a single erosion theory only regarding fluvial incision is not appropriate for channels that experience varying climatic conditions and sediment supply[46,76,79,82]. Especially periodic debris flows or hyperconcentrated flows are not included in these models but are assumed to contribute to massive scouring of bedrock channels[83-88] and might even play a substantial role in the formation of deeply incised alpine gorges[78,79].

The potential of bedrock erosion due to hyperconcentrated flows or debris flow compared to fluvial bedrock incision rates is still not yet systematically understood[50] due to a lack of quantitative observations[47], but it is assumed that abrasion and wear by particles in turbulent suspension play an important role[89-91]. Due to the substantially higher transport capacity, extreme events may be of great importance to bedrock channel erosion[5,44,82,92-94]. Also, it is unclear if the mechanisms controlling bedrock wear during flow conditions that are predominantly present in fluvial systems also influence the erosion during extreme flows with a substantial suspended particle load (hyperconcentrated flows). Most long-term bedrock incision rates can not be explained by the present short-term measured fluvial incision rates. A process with a higher erosion capacity is necessary. Yet, prior studies were seldom able to accurately quantify the spatial distribution of erosion in bedrock channels. Also, the erosion could not be attributed to one specific flow event with extreme sediment transport (hyperconcentrated flow).

Here, we hypothesise that (i) hyperconcentrated flows cause massive erosion in bedrock channels, (ii) that this erosion is not influenced by turbulent flow indicators like the sinuosity or channel shape, (iii) that channel erosion in hyperconcentrated flows is effected by massive impacts of the suspended load exceeding the compressive strength of the bedrock and (iv) that repeated hyperconcentrated flows in the Late Glacial or other event periods can provide an actualistically proved process capable of producing massive bedrock incision and gorge formation.

We showed this by quantitatively comparing Light Detection and Ranging (LiDAR) pointclouds which were recorded pre- and post-event of a hyperconcentrated flow and comparing the calculated bedrock erosion to channel parameters along the whole 900 m long gorge. Simultaneously, we analysed photographs covering the entire extent of the affected bedrock channel and performed a magnitude frequency analysis for the calculated erosion volumes.

Results
Setting
The *Höllental* is the most deeply incised alpine valley in Germany situated right below the highest summit of the country, the Zugspitze, 2962 m a.s.l.
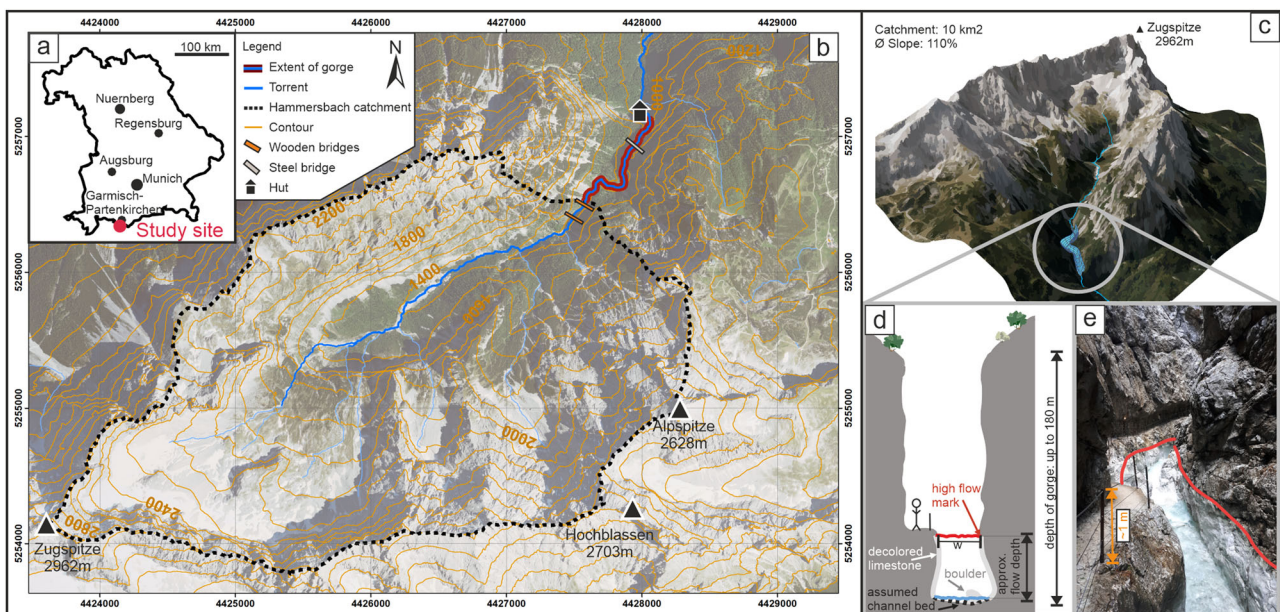

Fig. 1 | Overview of the study site. Location of the *Höllentalklamm* (red dot) near Garmisch-Partenkirchen at the southern border of Bavaria, Germany (solid black line) (**a**). **b** Superficial catchment (black dotted line) of the torrent *Hammersbach* contributing to the discharge at the gorge entrance. The Ridges northwest and south of the torrent range from 2000 to 2962 m a.s.l. including Germanys's highest summit Zugspitze. **c** 3D view of Germany's steepest catchment *Höllental* with a Ø 110% steep slope. **d** Sketch of a cross-section of the gorge with the relevant measured parameters. **e** Eroded decolored limestone gorge after the hyperconcentrated flow event (red line), the metal poles of the railing measure 1 m (orange arrow). Satellite data: Bavarian Surveying and Mapping Authority.

Article

(above sea level) (see Fig. 1). Its torrent, the Hammersbach, lies between two mountain ridges, and flows in north-eastern direction. It drains a catchment of ~10 km² with an extremely steep mean slope gradient of 110%. At the end of the north-eastern side of the valley, the torrent is forced through an up to 180 m deep, narrow gorge with varying widths between 1.3 m and 14.9 m. Upstream of the gorge, the torrent flows around 700 m with a gradient of 12.1%. Higher up, it originates from one of the tributary valleys of the north facing slopes. The channel bed at the upper entrance of the gorge lies at 1167 m a.s.l. and the torrent continues down through the gorge for 900 m with a steep mean gradient of 15.5% until the lower exit at 1010 m a.s.l. Since there is a substantial change in the slope, the gorge can be divided into two parts: The upper one is roughly 560 m long and has a gentler gradient of 10.7% and the lower one is with 380 m shorter and steeper (22.6%). Downstream of the gorge exit, the channel and the low part of the valley widen and the channel continues with a mean slope of 8.7% up until the settlement. The whole catchment above the gorge as well as the gorge itself consist of the homogeneous Triassic limestone *Wettersteinkalk*[95–97] characterised by extensive karst systems[98]. The rock strength of the predominant *Wettersteinkalk* was determined at 91 ± 27 MPa (Uniaxial compressive strength) and 7.2 ± 1.9 MPa (Uniaxial tensile strength) in Brazilian tests[99]. The area around the Zugspitze along with the *Höllentalklamm* constitute one of Bavaria's most frequented alpine tourist destinations with up to 2000 visitors per day. This investigation focuses on the geomorphic changes caused by a hyperconcentrated flow event of the 13th of June 2020. Triggering factor was a locally confined high precipitation event with 50–60 mm/h (DWD, Radar measurements) mobilising large amounts of sediment in the upper part of the catchment and forming a 60,000 m³ hyperconcentrated flow lasting for ~1 h (Wasserwirtschaftsamt Weilheim, written report, 2020). For comparison, a 1 h event with a precipitation sum of 51.2 mm has an statistical annuality of 100 years (KOSTRA, DWD). Most of the sediment which was mobilised during the event originated from rockfall deposits or scree slopes of a tributary valley that was heavily affected by the rainstorm and some was already in the vicinity of the upper exit of the

gorge. Documentation after the event showed a massive deposition of material above the entrance of the gorge as well as major geomorphological alterations in the bedrock channel of the gorge, both indicating the hyperconcentrated nature of the flow[87,100]. The deposited sediment at the upstream entrance of the gorge mostly consisted of sand and gravel with distinct layers between 5 and 30 cm height which themselves are poorly sorted. Downstream, most of the sediment was deposited in the less steep part of the channel close to the village *Hammersbach*. It also consisted mostly of gravel and sand and was quickly removed by excavators after the event. In the gorge itself, boulders up to 20 m³ were shifted over 15 m, in most parts the bed, sediment was cleared out completely and the channel looked white (like sand-blasted) with a visible high flow mark due to the high forces acting in the confined channel.

Massive erosion and transport

The hyperconcentrated flow event produced clearly visible geomorphic changes along the entire flowpath in the small timeframe of the event. Abrasion, plucking and shearing processes probably acted simultaneously on the bedrock walls and bed. Driving forces of the flow mobilised the only partially present thin layer of sediment inside the channel but also shifted or even disintegrated large boulders previously sitting in the channel. Some examples of the visible resulting changes due to the hyperconcentrated flow are shown in Fig. 2. A large boulder of 20 m³ was shifted downstream 16 m until it was lodged between a narrow part of the channel (Fig. 2 aI, aII). The bridge itself was not affected by the flow because it was above the hyperconcentrated flow height. In a majority of the affected areas where the hyperconcentrated flow eroded the bedrock walls of the gorge, a quantification of the erosion depth is only possible by comparison of the recorded laser scan point clouds (see "Change detection and volume calculation"). Only where large rock fragments were removed from the channel sides, we were additionally able to visually determine the scarp by comparing pictures pre- and post-event (Fig. 2 bI, bII). The largest detached rock fragment has a volume of 3.5 m³ and a maximum erosion depth of 1 m (lateral erosion

Fig. 2 | Examples of boulder transport and detachment of large rock fragments from the bedrock gorge walls. Pre-event pictures on the 28th May 2020 show the state of the gorge before the hyperconcentrated flow (upper row) and pictures from the 19th May 2020 six days after the event (lower row), respectively. All pictures are facing upstream. **aI, aII** A 20 m³ large boulder (yellow, dashed outline) was transported 16 m downstream until it was lodged between the narrow part between the rockwalls. **bI, bII** A 3.5 m³ large rock fragment (red, dashed outline) eroded from

the rockwall. It has a vertical extent of 1.5 m and a maximum erosion depth (horizontal distance) of 1 m. **cI, cII** show a section of the channel that experienced a high change in its boulder distribution. The central boulder in (**cI**) remains in almost the same position. Three boulders were transported downstream or disintegrated until unidentifyable (red, dashed outline). Two boulders (i and ii, yellow with dashed outline) were shifted or rotated but stayed in the same area.

depth, perpendicular to the flow). Most of the 1–3 m³ loose boulders that were mobilised during the flow were probably disintegrated since we could not trace them further downstream. Only in a few cases we managed to identify toppled or only slightly shifted boulders as seen in Fig. 2 cI, cII. The central boulder in cI was slightly rotated towards the camera position but did not experience disintegration. The surrounding boulders behaved in two possible ways: Some of them were apparently shifted further downstream and most likely disintegrated during that flow (highlighted in red) and some seemingly just changed their position but stayed in the closer area in the channel (highlighted in green with black arrows).

Change detection

Using the Multiscale Model to Model Cloud Comparison (M3C2) analysis[101], we were able to detect 232 eroded volumes that were rated statistically significant (see Fig. 3). The total volume of laterally eroded bedrock amounts to 20.60 m³ detached from a total area of 137.01 m² (only detected erosion areas with significant change). Thus, 2.4% of the scanned bedrock area affected by the hyperconcentrated flow (whole area below high flow mark including areas of erosion and non-erosion: 5708 m²) were eroded. The values for the three parameters volume, area, and mean M3C2 distance range over 1–5 orders of magnitude. Figure 4a shows the locations of detected erosion along the channel from a bird's-eye view as a heatmap and the boundaries between 10 m-sections of the channel. The corresponding values for the cumulative eroded volumes along the flow path, the flow depth in the channel and the elevation of the channel bed are displayed in Fig. 4b, dependent on the distance from the gorge entrance. A majority of the channel surface experienced lateral bedrock erosion, only in ~30% of the recorded channel, we did not detect quantifiable changes with the laser scanner. More than 33% of the volumetric bedrock erosion occurred between 420 and 500 m downstream which constitutes only 10% of the
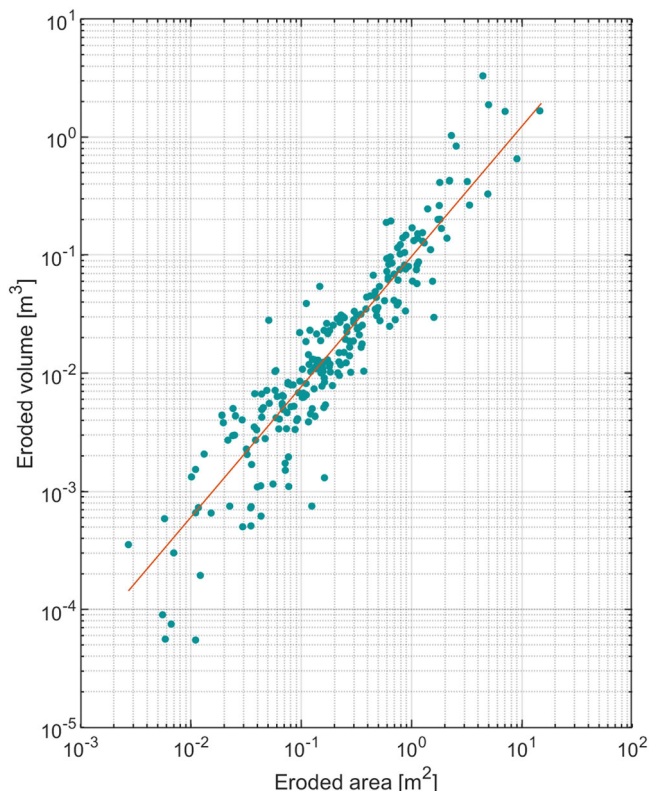
channel length. This section was precharged with some boulders, probably affecting the erosion pattern in their vicinity. We marked this part of the channel as the part with the highest erosion in Fig. 4a. Except for the lowest part of the gorge, only small volumes contribute to the total erosion volume up- and downstream of the central part. The largest eroded particle has a volume of 3.3047 m³ and it is located between 420 and 430 m downstream. It also sets the maximum mean erosion depth (mean M3C2 distance of one single volume) of 60.11 cm. At this location, the channel is only about 4 m wide and therefore, the flow widened the channel by ~15% in this area. Out of the 232 volumes, a very high proportion of small ones and only a few very large ones are contributing to the bedrock erosion, as the mean values for the volume and the area are considerably larger than the median (Supplementary Table 1).

To visualise the bedrock erosion along the entire flow path of the gorge, we divided the channel into 10 m-sections and calculated the erosion depth [mm] of each section by dividing the total eroded volume [m³] by the scanned pre-event area [m²] below the mapped flow height. The results are shown in Fig. 4c. Only in 27 of the 89 sections, no erosion was detected by the Cloud-Comparison. For the other sections, the mean erosion ranges from 0.018 mm to 42.97 mm. The mean erosion of the sections with detected erosion is 4.89 mm (median 1.69 mm) and 3.41 mm (median 0.76 mm) for the whole channel including the areas with no detected erosion. The four sections with the apparent highest erosion rates are located between 400–500 m and at 850 m channel length. The maximum erosion rate of the whole channel was detected at 42.97 mm in the section between 490 and 500 m downstream. We divided the data into 10 cm bins from the channel bed (defined as the baseline with the lowest recorded points in the laserscan, sampled at 1 m intervals) to analyse the erosion rates in dependence to the elevation from the channel bed. Figure 5a shows the distribution of the total scanned area [m²] varying over increasing height as well as (b) the total area of detected erosion and (c) the total volume of eroded rock fragments. Figure 5d displays the mean erosion for the whole channel dependent on the elevation from the channel bed. This value is obtained by normalising the height-dependent eroded area by the scanned area to avoid bias due to varying coverage of the point cloud. The highest erosion rates are reached between 1 and 1.4 m above the channel bed and range between 13.4 and 14.1 mm for the 1-h event.

Influence of local channel geometry

We calculated seven physical channel parameters for each of the 89 sections as well as the boulder density to account for blocking (See also Supplementary Table 2). The average width of all 10 m-sections ranges from 2.00 to 11.31 m throughout the flow path. Figure 4d shows the channel width sampled at a 1 m interval along the stream, as well as the deviation of each 10 m-section from the neighbouring sections and from the general valley orientation in the vicinity of the gorge. The maximum deviation of 121.25° from the valley orientation was calculated for the section between 240 and 250 m, marked with a pink star. Figure 4e shows the boulder density [m²/m²] in each section which is calculated by dividing the channel area covered by boulders (projected on the x-y-plane) by the estimated total bed area per section. The boulder density increases considerably towards the lower part of the channel but is highly variable. For each of the seven physical geometric parameters we tested the section-wise correlation with the mean erosion depth of the rock fragments [mm] (see Fig. 6), the total erosion volume [m³] and the mean M3C2 distance [m] of the detected volumes. For all 21 correlation tests indicative of turbulent flow, we did not find any trend or dependency as previously assumed due to typical local erosion behaviour in turbulent flows.

Magnitude-frequency distribution

We analysed the data set of 232 eroded rock fragments for the volume, eroded area, and mean M3C2 distance of each delimited fragment with regard to their magnitude-frequency distribution (see "Change detection and volume calculation" and "Statistical analysis"). Figure 7 shows the empirical magnitude-frequency distribution of the kernel estimation for all
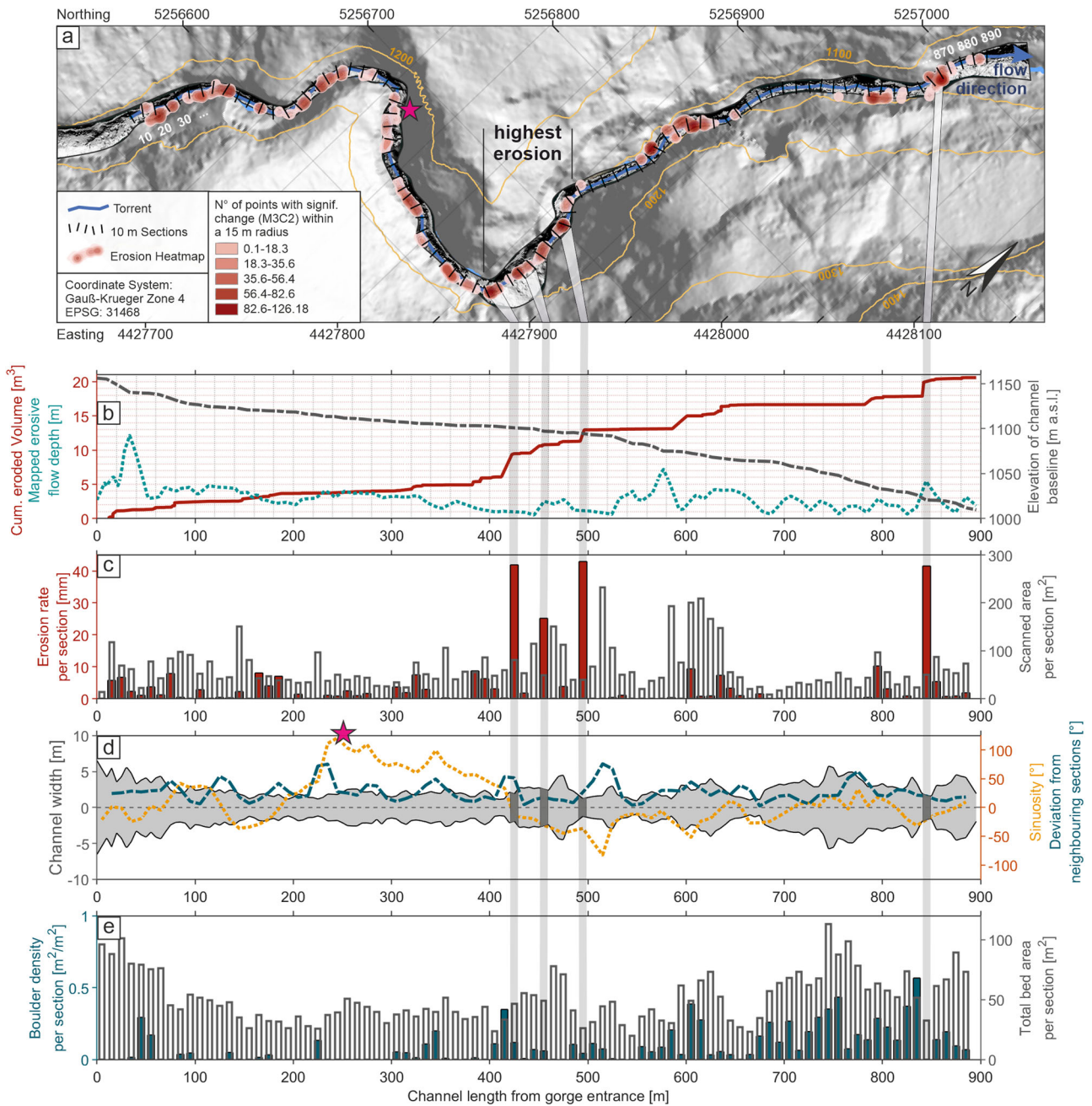

Fig. 3 | Volume-area plot of the eroded rock fragments. The volume–area plot of the 232 eroded rock fragments over 5 magnitudes detected by the change detection shows a power relation in the form $V = \alpha A^\beta$ with $\alpha = 0.097$ and $\beta = 1.11$. This power relationship is fitted by robust linear regression of the logarithmic transformed values of V and A.

Fig. 4 | Overview of the eroded areas and channel parameters in the *Höllentalklamm* along the flow path of the bedrock channel. a Density of detected points of lateral bedrock erosion by pointcloud comparison (heatmap). The black lines orthogonal to the flow path mark the transitions of the 10m sections. (Underlying DEM: Bavarian Surveying and Mapping Authority, 2006). **b** Cumulative volume of all detected erosion-volumes from the change detection along the flow path (red solid line) and the elevation of the channel baseline with the lowest recorded points in the laser scan (grey dashed line) with the mapped erosive flow depth (blue dotted line) calculated as the difference of the high flow mark to channel bed. **c** Bar plot of the lateral erosion rate (red bars) per section which is calculated by normalising the eroded volume with the scanned pre-event areas (grey hollow bars) actually affected by the flow in every section (below mapped flow height). The four sections with the highest erosion rates are connected to the other panels by grey bars to show the corresponding values in the other graphs. **d** Channel parameters along the flow path: Channel width in [m] measured in 1m-intervals (grey area), sinuosity [°] as the deviation of every 10 m-section from the general valley orientation in the region of the gorge (33.69° azimuth) (yellow dotted line) with the hightest deviation of 121.25° marked with the pink star, and the deviation [°] of each section from their neighbouring sections (blue dashed line). **e** Boulder density [m²/m²] (blue bars) in each section calculated by dividing the projected (on the x-y-plane) area of boulders in the channel by the estimated bed area (grey hollow bars) per section.

three parameters. All have the characteristic form with a rollover and a power-law tail. This indicates that the largest volumes have a low frequency whereas there is a high frequency of small volumes to be eroded. The values of β and γ obtained from the robust linear regression (RLR) are consistently smaller than the ones of the maximum likelihood estimation (MLE) (for methods see "Statistical analysis"). The p values of all power-law models of

the three datasets are much higher than 0.1 indicating a good fit to the data[102]. Testing the robustness of the power-law fit by a bootstrapping simulation produced 95%-confidence interval of the power-law exponents β and γ. Results show minimal variations for the RLR of the cumulative distribution function (CDF) and the probability density function (PDF) for the datasets and reasonable variations for the MLE (Supplementary

Fig. 5 | Relation between erosion and elevation from channel baseline. Dependence of the average erosion of the whole channel affected by the hyperconcentrated flow to the elevation from the channel baseline (lowest recorded points in laserscan). **a** Distribution of the total area recorded by the laserscan [m²] in relation to the distance to the baseline. **b** Total of the eroded area [m²] detected by the pointcloud-comparison in relation to the height above the baseline. **c** Total of the eroded volume [m³] detected by the pointcloud-comparison in relation to the height above the baseline. **d** Mean erosion depth [mm] for the whole channel in relation to the height above the baseline. The values are calculated by normalising the eroded volume [m³] with the total of the scanned area to avoid bias due to a varying point density of the scan.
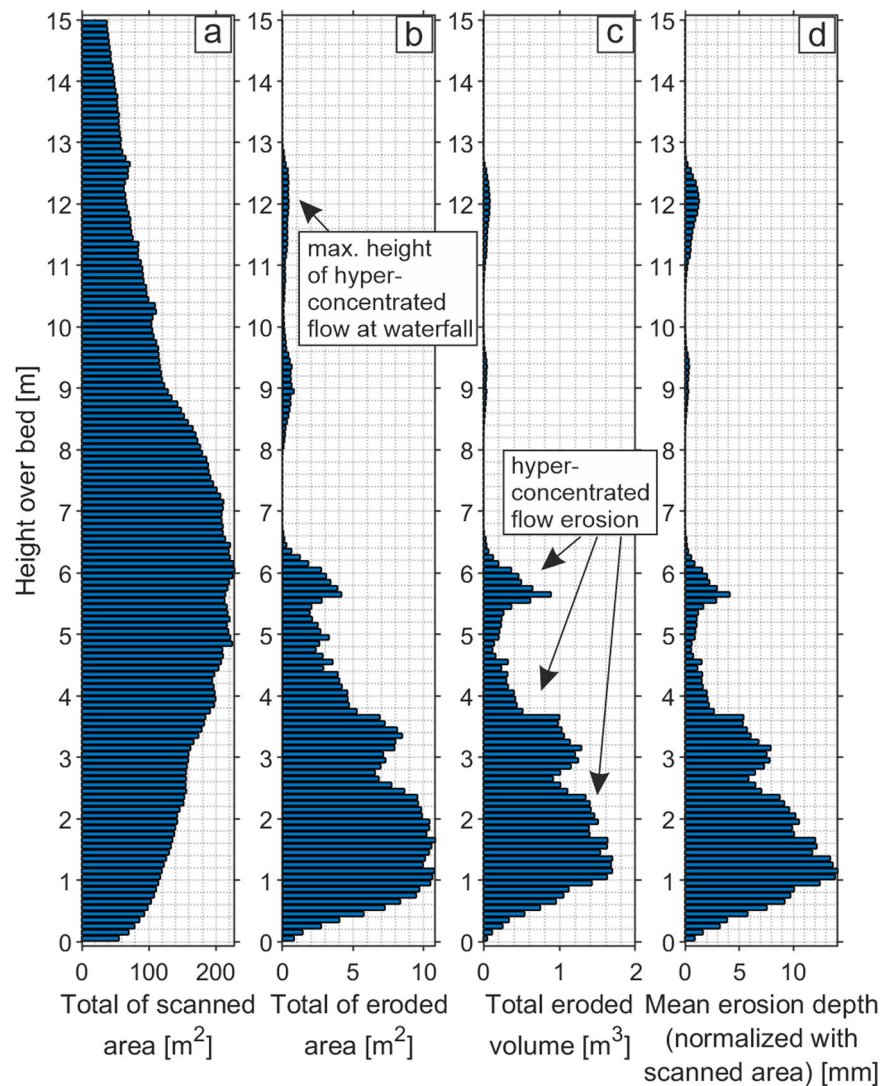

Table 3). x_{min} was obtained by the MLE and defines the lower limit of the tail where all values larger x_{min} follow the power-law distribution. x_{min} being 0.08 m³ for the volume dataset (0.59 m² for the area dataset; 0.05 m for the M3C2 distance dataset) means that 19.8% (26.3%; 31.9%) of the 232 rock fragments are in the tail which constitutes 85.8% (81.2%; 60.7%) of the total volume (area; eroded distance M3C2).

Discussion
Discussion of methodology and error sources
Limitations of the change detection analysis refer to data acquisition and processing. Occluded areas in the up to 2 m narrow *Höllentalklamm* are inevitable and the complex geometry with numerous bends (Fig. 1) challenges the laser scan coverage. We minimised these effects by recording >80 scan positions and oblique measurements. Coverage of the channel bed below water was restricted due to the constant water flow pre- and post-event. We assume the data is representative for the entire bedrock surface of the channel as detected changes are equally distributed along the entire flow path (Fig. 4) and in various heights above the channel bed (Fig. 5). We hypothesise that our value for vertical incision is a minimum estimate as vertical erosion rates can be up to three times the lateral rates[36]. Thin erosion depths are presumably underrepresented as the pointclouds' limit of detection ~2 cm without using ground control points in the gorge. This uncertainty is intrinsic to the method and describes the maximum achievable LiDAR accuracy on a structured rock face[103]. Therefore, the values of

lateral erosion shown here are a conservative minimum. However, this study concentrated on massive fragmental erosion on rock faces along the gorge considerably exceeding the mm abrasion along the channel. Considering this, we gain a major advantage by using LiDAR measurements instead of a point measurement technique (e.g., refs. 12,104) in the channel obtaining areal retreat rates along 100 million data points. Probably the main limitation of our analysis is the finite nature of the available data. The hyperconcentrated flow lasted for a maximum of 1 h and we are fortunate enough to have gained data 2 weeks prior. It is beyond the scope of any study to observe such an event a second time and generate more data. Despite the limitations stated above, the data set and the subsequent analysis of the erosional capacity of the flow are unique and provide unparalleled insights into highly erosive flow processes. To our knowledge this is the first data set of an entire bedrock channel (5708 m² analysed surface) that allows the calculation of in-situ erosion of bedrock surfaces due to a natural extreme precipitation event leading to a hyperconcentrated flow. Remarkable features of the analysis are: (i) We were able to quantitatively detect changes caused by the hyperconcentrated flow at numerous locations in the bedrock gorge along the geometrically varying channel. (ii) A clear identification of the responsible process is given by the short time frame of the acquisition period and the detailed mapping of the affected rock surface. Coalescence with other processes like rock-falls or other extreme discharge events can therefore be widely excluded. (iii) The volumetric changes detected by the cloud-comparison range over five orders of magnitude and represent
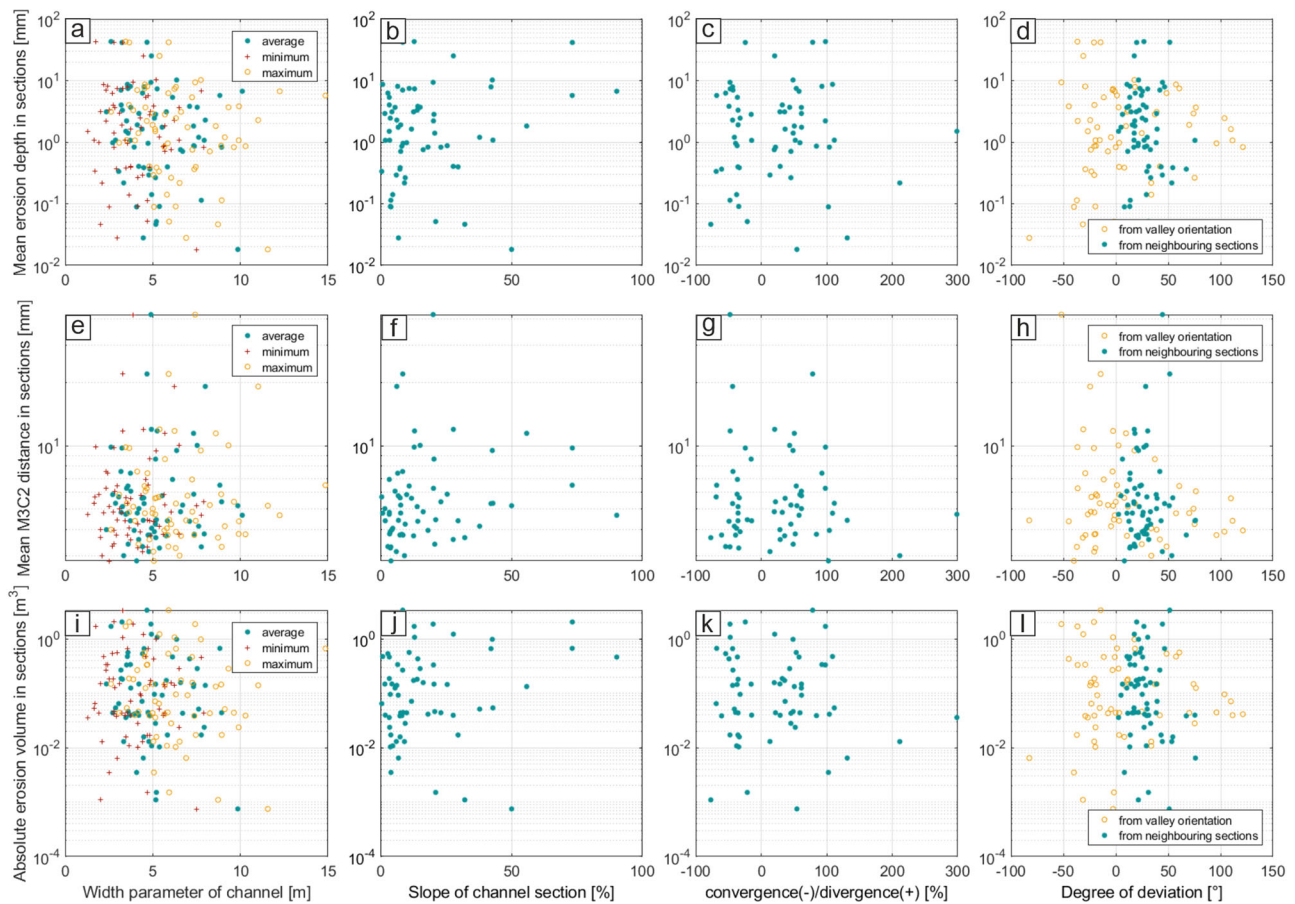
Fig. 6 | Semi-log scatter plots of erosion in relation to different channel parameters. Mean erosion depth [mm] (**a–d**), mean M3C2 distance [mm] (**e–h**) and total erosion volume [m³] (**i–l**) in the 89 single sections correlated to seven physical geometry parameters (see "Influence of channel characteristics"): Mean, minimum, and maximum width of the sections (**a, e, i**), mean slope of the channel section (**b, f, j**), percentage of convergence or divergence (**c, g, k**), and degree of deviation from the valley orientation as well as from the neighbouring sections (**d, h, l**).

different types of geometric shapes, indicating the quality of the dataset. (iv) The resulting erosion rates are calculated conservatively and represent minimum values.

The correlation analysis of the 232 eroded volumes to the channel geometry reflects the finite character of data sets and detection thresholds (Fig. 6). The results of the present data do not disprove that changes smaller 2 cm erosion depth follow a local erosion pattern that is similar to fluvial bank erosion[62–67]. 10 m sections of the rock gorge account for the detectable size of eroded volumes and the complexity of the channel. The varying channel geometry does not have a considerable influence on the erosion for the analysed volumes with mean erosion depths between 2 and 60 cm. We hypothesise that normal stresses act more or less uniformly on the bedrock surface of the gorge, independent of the absolute flow height or geometry, due to the enhanced particle collisions in the heavily sediment-laden flow. Although the analysis of the local (section-wise) slope did not give any results, we do not exclude the influence of the reach-scale slope. As seen in Fig. 4b, there is a change of slope around 560 m along the channel of the gorge. A large proportion of the erosion is located directly upstream of this gradient change. Nevertheless, the whole gorge can be seen as the knick-zone (slopes up- and downstream are less steep) and the analysis done in this study focuses on the local erosion patterns as well as the magnitude.

The consistent distribution in the magnitude-frequency analysis (Fig. 7) supports the hypothesis of equal distributed erosion inside the hyperconcentrated flow. The magnitude-frequency ratio of eroded rock fragments, i.e. β and γ for the volume dataset, both obtained with maximum likelihood estimation as well as the linear regression, are surprisingly consistent with previous rockfall/rock slope failure studies[105]

corresponding to the upper limit of parameters obtained for rockfall data-sets. The common magnitude-frequency analysis of mass-movements focuses on the volume[105–109], however, due to the excessive data on erosion we can also show similar fits for eroded particle area and eroded depth. With 232 analysed volumes only a proportion of them follow the power-law distribution of the tail, some grade of uncertainty is unavoidable. However, the data sets exhibit a reliable power-law behaviour and the rollover is a product of resolution because smallest volumes have an erosion depth close to the detection limit. We conclude that the erosion pattern of the gorge induced by hyperconcentrated flow event does not act in the same way as turbulent flow erosion laws but rather mimics a mechanically enhanced rock wall retreat of the channel walls.

Erosive power of turbulent flows vs. hyperconcentrated flows
In turbulent flows, sediment transport is mainly limited to a distinct layer near the bed whereas hyperconcentrated flows are characterised by a high sediment percentage transported in suspension throughout the water column[87]. To compare the erosive power of these processes, we highlight five features in which both show particular behaviour.

(i) Erosion efficiency: The erosion efficiency of a single process is very difficult to quantify. Since the incision in bedrock channels usually extends over periods that range in geological timescales, measurements of in-situ erosion is challenging or limited to extreme events[4,5,8], weak bedrock[110], controlled flooding[36] or extremely high uplift rates[55]. An overview of some estimated long-term incision rates in bedrock channels can be found in ref.[111] whereas newer studies calculated long

Fig. 7 | Distribution fitting of the erosion data.
a–c Cumulative empirical distributions for the data sets V, A and D with theoretical power law models by the maximum likelihood method (MLE) represented by the solid red line and robust linear regression (RLR) of the cumulative distribution function (CDF) (dash-dotted black line) and probability densitfy function (PDF) (dashed yellow line). **d–f** Empirical frequency distributions (PDFs) for the data sets V, A, and D with theoretical power law models from robust linear regression of the PDF (dashed yellow line).
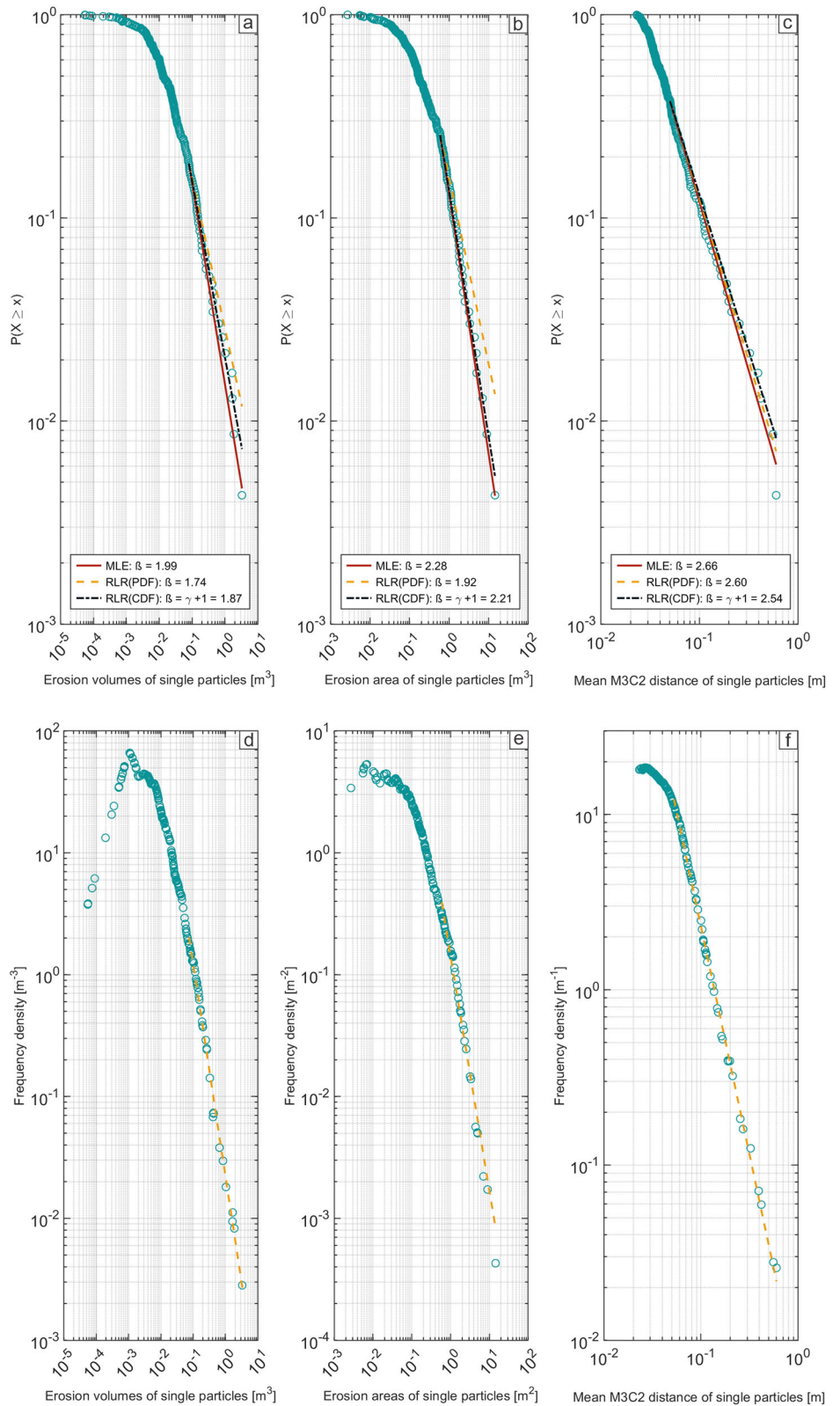
term bedrock incision rates by cosmogenic nuclide dating (e.g. refs. [112,113]. As seen in prior studies, the calculated long-term bedrock incision rates in different lithologies and climate usually greatly exceed the measured short-term incision at the respective sites[23,45,104,114,115], indicating a higher historic erosion capacity, maybe dominated by one or more likely several extreme events, than the present one (see also

Supplementary Tables 4 and 5). The measured erosion rates in ref. [36] were acquired using a similar technique to this study and represent erosion due to induced flushing by a hydropower company with a total of 208 events with varying sediment loads. The resulting mean lateral erosion rate measured over the 2 years of turbulent flows with moving bedload is 0.4 mm/a. In comparison, the mean lateral erosion of the

bedrock walls in this study in the *Höllental* gorge is 8.5 times higher (3.41 mm) generated by only one hyperconcentrated flow event. Supported by the above stated studies of short- and long-term incision and the disagreement of the magnitudes we postulate that turbulent flows carrying sediment only in the lower water column near the bed are not the effective process in eroding bedrock channels. In comparison extreme events like hyperconcentrated flows with particle collisions in the whole flow column are a major contributor to the deepening and widening of these bedrock channels.

(ii) Erosion pattern: Our observations lead us to the assumptions, that erosion patterns for hyperconcentrated flows differ from turbulent flows. The highest erosion rates were found in boulder pre-charged sections of which one was located between 400 and 500 m channel length in the *Höllental* gorge (see Fig. 4). By mobilising the complete stored sediment in the channel, the hyperconcentrated flow surpasses the cover effect of turbulent flows and assumingly is able to erode all bedrock surfaces efficiently. As seen in ref. [36], vertical incision exceeds lateral erosion and therefore it is highly probable that this is also the case at the *Höllentalklamm*. The analysis of the channel geometry supports this theory since we were not able to find any correlation between the erosion [mm] and the different channel parameters in the 10 m—sections. Figure 5 shows the pattern of the erosion-height dependency: The highest mean erosion depths are found at ~1–1.5 m above the channel baseline. The decline of erosion below this height could be due to a temporarily raised sediment bed (cover effect) in parts of the channel but due to the minimal sediment coverage after the event the decrease is likely biased due to no data below the baseline and inherits some error potential. Another explanation could be that there was a sediment coverage during the flow but was flushed away in the aftermath. Between 1.5 and 5 m over the channel bed, the erosion almost continuously decreases. Above that, the flow only partially reaches these high flow depths and a small number of larger volumes constitute to the erosion depth. These results show that there is a vertical distribution with a decreasing mean erosion depth from 1 m above the baseline upwards to ~5 m above the baseline and still a substantial erosion capacity in the higher parts of the flow column.

(iii) Transport capacity: In turbulent flows, the transported gravel size in the moving or saltating bed load is directly related to the flow velocity. The bedload usually consists of sizes up to coarse pebbles mixed with finer grains. If there is sediment in suspension, it is restricted to silt and sand whereas the latter settles quickly for slower flow velocities. Due to the pronounced higher sediment concentration in the hyperconcentrated flow, the fluid density and viscosity are both increased[100]. Coupled with the steep gradient of the channel, this enables upward disperse stresses by particle-particle and particle-bedrock collisions and supposedly allows blocks as large as 20 m³ (see Fig. 2a) to be transported (rolled, toppled, lifted or a combination of those) in transient suspension.

(iv) Mechanical process: The most important mechanical erosion processes in turbulent flows include abrasion and fluvial plucking by the bedload particles[45,47,50,89]. Smooth channel surfaces as well as flutes, scallops and potholes are the result of fluvial abrasion which could be described similar to sand blasting[54,116]. The role of the suspended load in the flow regarding lateral erosion is substantial as pointed out by both experimental setups and mechanistic models (e.g. refs. [89–91]). In fractured rocks, hydraulic plucking from the bed and banks can be more efficient than abrasion[45,117]. Since rock fragments are chipped off the bed or the banks, the remaining surface is typically not rounded or smooth. Reaches carved in weak or highly fractured rock are commonly prone to be covered in plucked blocks and bedload, therefore limiting the incision[50,118] whereas reaches in massive rock are commonly shaped by abrasion with a great amount of exposed rock. Due to the increased transport capacity, the actual suspended sediment load in hyperconcentrated flows is substantially higher than in turbulent flows and also mean particle volumes are larger. We believe that the disperse

stresses and the shear stress due to the yield strength are the major drivers of the bedrock erosion in hyperconcentrated flows and act extensively on the entire wetted perimeter of the channel. A decrease of the sediment proportion in the higher part of the flow column is plausible and therefore results in a decrease of the erosion capacity (see Fig. 5). Innumerable particle-particle and consequently particle-bedrock collisions[100,119] act as a combination of enhanced abrasion and plucking[39,86], constantly chipping off smallest rock fragments and loosening larger blocks for detachment. Similar to debris flows with high fluid density and rapid flow velocities, the drag[120] and lift forces effortlessly extract the loosened rock fragments and immediately transport them downstream.

(v) Event magnitude: It is commonly assumed that for turbulent flows, the erosion processes of bedrock can be characterised as incremental wear (i.e. abrasion) of the weathering crust in a [sub mm] to [cm] scale[45,121] as well as detachment of smaller rock fragments (i.e. plucking) up thicknesses in [dm] scales[36]. This process is continuously shaping the bedrock channel and it takes years or several decades until changes are actually visible. In comparison, debris flows scour is assumed be more efficient as seen in laboratory and field experiments[119,122]. In the discussed event, we show that also hyperconcentrated flows are capable of breaking out rock fragments up to [m³] magnitudes and visibly changing the channel in less than 1 h. Owning such an increased erosion capacity compared to turbulent flows, hyperconcentrated flows might have a more relevant role in channel incision and especially in gorge formation than previously considered.

The geomorphological legacy of hyperconcentrated flow events in gorge formation

The results we gained from the analysis of the hyperconcentrated flow event in the *Höllental* gorge lead us to the assumption that this process does have a leading role in bedrock gorge formation and can have an accelerating effect on the incision rates due to its extremely high erosive power. This hypothesis is supported by the following aspects:

(i) As already discussed in several studies, explaining bedrock incision and gorge formation solely with fluvial incision is not realistic because it is not controlled by only one single process but instead by several interconnected physical processes[23,76,82,123]. As mentioned above, short-term measured bedrock fluvial incision rates fail to match the long-term averages in a number of catchments around the globe (Erosive power of turbulent flows vs. hyperconcentrated flows) and would therefore be inadequate for producing erosion rates that are capable to efficiently incise these bedrock gorges in the given timeframe. A process with higher erosive power is necessary to fill this gap.

(ii) In this study, we show that hyperconcentrated flows have the capacity to massively erode bedrock in the matter of a single event lasting 1 h. We calculated lateral erosion values as high as 43 mm per hour in some *boulder pre-charged sections* and 3.41 mm per hour averaged over the whole gorge.

(iii) If sufficient debris and water supply are present in the upstream catchment of the gorge, such repeated extreme events of hyperconcentrated or debris flows would be able to incise into the bedrock and form a gorge more quickly as it is currently known. The gorge is incised up to 180 m which would theoretically require a mean of 5 events/year similar to this study for 10k years to form if calculated with the conservative (minimum) erosion rate of 3.41 mm per event-hour. Events that last longer or transport more coarse sediment may even be more efficient.

(iv) Conditions today may not provide enough sediment or water supply to repeatedly produce events that effectively erode bedrock in a short time span. Lateglacial times however provided nearly unlimited sediment and water supply over 10^1–10^3 years after the beginning of the glacial retreat. This paraglacial period is characterised by glacial over-steepening, the redistribution of remaining debris in the valleys and a

resulting high geomorphological activity[17]. These periods of sufficient boulder, debris and water supply could be able to produce extremely high erosion rates similar to rates during other transient landscape responses[47,114,124].

(v) This is also supported by the theory, that bedrock incision is mainly occurring in comparatively short time-frames and channels are mostly being in a state of non-incision[125]. Therefore, most observations today (even measurements lasting several years) are only portraying very low incision rates due to the climatic and topographic conditions. The long-term incision rates are consequently higher since they average the periods with states of non-incision and high incision.

(vi) Further backing this theory are locations of late- and postglacial moraine deposits at the study site: All four gorges in the area, the *Höllental* gorge, *Partnach* gorge, *Mitter-* and *Hinterklamm* show a distinct pattern. Moraine deposits were mapped in the direct vincinity upstream or on top of these gorges[126]. The location of the gorges was therefore probably set by the furthest advance in the Older Dryas (ca. 14k before present (BP)) or Younger Dryas (ca. 12k BP), providing immediate sediment and water supply upstream. This pattern of gorges being in a paraglacial environment is found in many locations in the Alps and beyond[13,14,20,127,128] and extreme landscape response after a glacier retreat is well known[18].

Conclusions

We were able to directly observe a hyperconcentrated flow controlling bedrock erosion of a narrow limestone gorge in a qualitative as well as a quantitative way. Using pointclouds pre- and post-event, we identified 232 volumes eroded from the bedrock walls. Assessing the data in several aspects lead us to the following main conclusions:

1. To our knowledge this is the first dataset of a quantitative change detection demonstrating the geomorphic changes in narrow bedrock (limestone) gorge produced during a natural hyperconcentrated flow event.

2. We quantified the minimum erosion and transport resulting from a single event lasting only 1 h: A mean of 3.41 mm lateral erosion averaged over the whole affected channel as well as the maximum erosion of 43 mm in a 10 m-section is evidence for the massive erosion capacity of the hyperconcentrated flow event.

3. All turbulent flow indicators were proven to have no influence on the erositvity distribution in the channel for the given level of detection. The only dependence that is clearly visible is the mean erosion decreasing with increasing distance from the channel bed. The maximum erosion of 14.1 mm is recorded between 1.1 and 1.2 m above the channel bed.

4. Instead, we showed that magnitude frequency distributions of the eroded volumes mimic mechanically enhanced sub-aerial rock wall retreat of the channel walls. This means that the erosion is not governed by the flow conditions but rather dominated by the predisposition (e.g. fracturing) of the channel material.

5. We compared five erosion parameters of turbulent flows to hyperconcentrated flows. Due to erosion efficiency, pattern, transport capacity, mechanical process and event magnitude of hyperconcentrated flows, it is one of the major processes that is capable of producing erosion rates that can efficiently incise bedrock gorges. Therefore, extreme events with high sediment transport capabilities should certainly be included in landscape evolution models.

6. We postulate that extreme events like hyperconcentrated and debris flows have a leading role in the incision and genesis of alpine gorges and can accelerate gorge formation in periods of sufficient sediment storage upstream and water supply such as postglacial times.

Methods

LiDAR data acquisition and processing

Terrestrial LiDAR data acquisition was performed using a RIEGL VZ-400 laser scanner with ca. 150 million data points per scan campaign. Due to the exposed bedrock in the gorge, reflectivity was excellent at the channel sides and bedrock walls. The bed on the other hand was covered with the usual water flow which resulted in a poorer reflectivity and no or only sparse data of the solid or sediment-covered channel. Two LiDAR campaigns were conducted pre- and post-event. On the 28th of May 2020, 84 single scans were recorded at positions along the channel and are representing the morphology before the flow event. The post-event channel morphology was recorded on the 19th and 25th of June with a total of 89 scans. The scans were performed from the path proceeding through the whole 900 m of the gorge. Every resulting pointcloud overlaps with at least the previous and the following one to gain a continuous recording of the gorge and to ensure co-registration of the single scans. The angular step of the laser scanner was set between 0.04° and 0.06° with an angle measurement resolution below 0.0005°. The resulting point cloud resolution typically ranges between 1.4 and 2.0 cm at a 20 m distance. Data gaps due to occlusion are non-avoidable in this environment due to the overhanging rock walls and winding channel in the gorge due to the incision of the torrent.

For point cloud alignment, an iterative closest point algorithm[129–131] was applied in RiSCAN Pro 2.9. The algorithm identified plane segments in every point cloud and then minimised the differences of the planes normal vectors of two scans. By successively reducing the search radius, only areas that are not subject to geomorphic changes are used for the alignment[132,133]. The standard deviations of the co-registrations (Root mean squared error—RMSE) are generally below 1 cm due to the high resolution of the point clouds. Subsequent filters eliminated the sparse vegetation as well as erroneous data points[134] and point density reduced to 2.5 cm in XYZ-direction in order to prevent bias due to heterogeneous point densities. The data base for georeferencing (to get global coordinates and heights) is an airborne LiDAR dataset recorded in 2006 (Bayerische Vermessungsverwaltung—www.geodaten.bayern.de).

Change detection and volume calculation

In this study, we applied the Multiscale Model to Model Cloud Comparison (M3C2)[101], a direct distance calculation[135,136] rather than the calculation of displacement fields by identification of corresponding objects[137,138] as it is better suitable for complex terrain such as the rock faces of a meandering gorge. Subsequently, we calculated the corresponding volume by triangulation and projection of the single-volume point clouds. M3C2 computes a normal vector for every point of the reference cloud (1) by fitting a plane of a specified radius D/2 to all the points inside this area. Subsequently, a cylinder of a radius d/2 oriented along the normal vector is defined and a maximum cylinder length is set. The intercept of the two clouds (1 and 2) with the cylinder produces two subsets of points which are used to calculate a mean point position in each subset and therefore calculate the measured distance (LM3C2). Confidence intervals (level of detection, LOD95%) are obtained by combining the standard deviations σ_1 and σ_2 of the point distributions within the cylinder with the alignment uncertainty to quantify the distance measurement accuracy. σ_1 and σ_2 include errors produced by instrumental uncertainty, surface roughness and alignment uncertainty[139,140]. Detected surface change is then either rated statistically significant (LM3C2 > LOD95%) or rejected (LM3C2 < LOD95%). The change detection analysis and volume calculation were carried out in CloudCompare and RiScan Pro 2.9. Due to the insufficient point density along the channel bed, we omitted the analysis of the incision of the bed and focused on the lateral erosion of the bedrock walls. Optimising accuracy, we divided the point cloud of the gorge in left and right side of the torrent and set a normal scale (D) of 1 m, a projection scale (d) of 0.5 m and a maximum cylinder length of 3 m for the analysis. The correct direction of the normal vectors towards the channel was defined by using the scanner positions as orientation points. Distance calculation produced negative values for bedrock erosion and positive values for probable sediment deposition. All areas of significant surface change (LM3C2 > LOD95%) were validated manually for plausibility with photographs (for exemplary M3C2 results, see Supplementary Fig. 1). For each area, where erosion could be detected either as a breakout of rock fragments or due to abrasion processes (both named eroded volumes or rock

fragments in the following), the corresponding points of both clouds were isolated (PP1 and PP2). Area and volume calculation of each eroded rock fragment was carried out with the Cut and Fill tool in RiScan Pro (similar to ref. [141]). The isolated point clouds PP1 and PP2 were triangulated to create two meshes and projected on a plane that is parallel to the surface of the rock wall. This results in the area value for every one of the 232 detected locations of significant erosion. The volume is then calculated by subtracting the calculated volume between the post-event mesh and the reference plane from the volume between the pre-event mesh and the reference plane. Additionally, we computed the mean erosion depth of every eroded area as the mean of the calculated M3C2 distances between the corresponding point clouds.

The erosive flow height (high flow mark) of the hyperconcentrated stream (total flow height might be higher, but there is no indication about that) is witnessed by a rock surface colour change induced by erosion processes throughout the whole gorge. Therefore, we recorded the whole length of the gorge with a 360° camera to document these visual changes. All eroded volumes detected above this erosive flow height were removed from further analysis since the responsible process is potentially not the flow but rockfall. By determining the erosive height of the hyperconcentrated flow, we were also able to calculate the scanned area of the bedrock walls that were affected by the event by projecting the pre-event pointcloud to planes parallel to the mean rock surface. We calculated an accurate mean erosion for the whole channel and section-wise along the channel. For this, we divided the channel of the gorge into 10 m-segments along the channel axis, resulting in a total of 89 segments, the respective fractions of the pointcloud, and a simplified channel axis with nodes at the section-borders. The channel axis represents the channel bed (defined as the baseline) with the lowest recorded points in the laserscan, sampled at 1 m intervals. We carefully identified this baseline manually to not encompass any boulders or larger sediment piles in the channel.

Influence of channel characteristics

To test if the longitudinal variations in channel geometry influence the erosion rates similar to turbulent flow conditions[60–63,73], we analysed key attributes along the channel using the same 89 10 m-segments as described above and correlated them to the erosion rate in the respective sections (Supplementary Table 2). For each segment, we calculated seven physical parameters from measurements of the coordinates in the globally registered pointclouds: (1) The width was measured perpendicular to the channel axis every 1 m at the high flow mark in the pre-event pointcloud and then averaged for the 10 m sections to obtain w_{av}. Also, the (2) minimum (w_{min}) and (3) maximum (w_{max}) measured width was extracted. (4) The average slope Ø s represents the gradient between the nodes of the simplified channel axis in each section and is therefore sampled every 10 m. (5) We analysed manually if the section has a convergent (channel width downstream gets smaller) or divergent (channel width downstream gets larger) behaviour and computed the percentage of narrowing (con) or widening (div) from the relation of (w_{min}) and (w_{max}) (e.g. if the channel widens from 1 m to 1.5 m the result is a divergence of +50%) (6) For the curvature c, we calculated the deviation of each channel-axis segment from the previous and the subsequent one and added up both values. (7) The sinuosity sin, hereby defined as the deviation from the general valley orientation in the region of the gorge (33.69° azimuth) was also calculated using the single segments of the channel axis. To correlate these parameters to the mean erosion normalised by the scanned area, mean M3C2 distance and total erosion volumes, we manually assigned all 232 eroded volumes to the respective sections and created scatter-plots with the channel parameters versus the respective erosional parameters. Additionally, we calculated the boulder density in each section. To account for the bed area covered by boulders we clipped the parts of the pointcloud from Mai 2020 so that only boulders sitting in the channel were left. We then triangulated the pointcloud to create a mesh and divided the result into the same 89 10 m-segments. For every section we performed a projection by rasterising the meshes in 0.1 m cells

and subsequently calculated the area [m²]. To get the percentage of boulder coverage, this value was divided by the estimated total bed area [m² per section (average channel width multiplied by the section length).

Statistical analysis

Due to the visual similarity of the analysed data set to rockfall inventories, we used statistical analysis tools such as magnitude frequency distributions, that are common for landslide inventories. Many landslide and rockfall monitoring studies showed the power-law behaviour of the magnitude frequency relation above a certain size x_{min} and a possible rollover below x_{min}[105–109,142–147]. A power law distribution can accurately describe the probability distribution of datasets that range over several magnitudes. In our case we investigated the assumption of a power-law behaviour with three parameters which we quantified for each erosion particle: Erosion volume V, erosion area A and mean M3C2 distance D. To check whether the data follows a power law distribution in the tail, we analysed magnitude-frequency relation in two ways, similar to earlier studies[105,146]: Calculating the CDF and the PDF. The PDF is considered as a better visualisation of a possible rollover but simultaneously more prone to a bias introduced by the user selection of bin sizes[102,148]. Therefore we applied both CDF and PDF approaches and fitted the tail of the CDF to a power law function using a maximum likelihood estimation MLE[102]. If a parameter x of interest follows a power law, the PDF can be defined as:

$$f(x) = ax^{-\beta} \qquad (1)$$

Where $f(x)$ is the frequency, α is the normalisation constant and β is the power-law exponent. As mentioned, this method involves binning of the values to compute the probability. Additionally to a histogram, we used a kernel density estimate which in comparison is more robust against any variations in the frequency[149]. We obtained best results for the PDF using a box kernel with widths of 0.4 to the log-transformed parameter values. The CDF can be described by the integral of Eq. (1):

$$F(x) = P(X \geq x) = \left(\frac{x}{x_{min}}\right)^{-(\beta-1)} = \left(\frac{x}{x_{min}}\right)^{-\gamma} \qquad (2)$$

Where $F(x)$ is the probability, that the value of an arbitrarily chosen value exceeds x, $xmin$ represents the lower bound of the values that are contained in the power-law distribution and $\gamma = \beta - 1$ is the slope of the CDF. We then estimated β by three methods (similar approach as described in ref. [105]): (1) Fitting β and x_{min} to the CDF using the MLE[102] (2) a robust linear regression of the CDF and (3) a robust linear regression of the PDF of the logarithmically transformed frequency and parameter values. For the estimation using methods (2) and (3) we used the resulting x_{min} calculated by the MLE of method (1) to define the lower limit of the parameters above which the power-law distribution of the data starts. Values below the defined threshold x_{min} were excluded from the linear regressions. The objective estimation by method (1) also allows for the calculation of the p value which is the likelihood of a power-law distribution of the tail. For this purpose, the distances of 1000 synthetic datasets to the hypothesised power-law distribution are calculated. The p-value then represents the fraction of distances that are larger than the distances of the empirical dataset. If $p > 0.1$ the power-law hypothesis is valid[102]. Similar to earlier analysis of power-law distributed data[146,147] we tested the sensitivity of the parameters with a Monte Carlo simulation. Different bootstrapping approaches were used for the methods (1)–(3): To calculate the 2.5th and 97.5th percentile (95% confidence interval) of the estimates by the maximum likelihood method (1), we randomly removed 10, 20, and 40 eroded volumes of the whole dataset and resampled it 10,000 times respectively. To obtain the sensitivity of the exponent estimated by methods (2) and (3), 20% of the volumes larger than x_{min} (volumes in tail) were removed and the dataset resampled 1000 times, each time repeating the identical linear regression.

Article

Data availability

Source data of the graphs, pointclouds of the (significant) M3C2 change detection as well as pointclouds of the single eroded bedrock volumes are deposited under the following permanent link https://doi.org/10.14459/2024mp1735961.

References

1. Wolman, M. G. & Miller, J. P. Magnitude and frequency of forces in geomorphic processes. *J. Geol.* **68**, 54–74 (1960).
2. Karlstrom, K. E., Crow, R., Crossey, L. J., Coblentz, D. & van Wijk, J. W. Model for tectonically driven incision of the younger than 6 ma grand canyon. *Geology* **36**, 835 (2008).
3. Gupta, S., Collier, J. S., Palmer-Felgate, A. & Potter, G. Catastrophic flooding origin of shelf valley systems in the english channel. *Nature* **448**, 342–345 (2007).
4. Lamb, M. P., Dietrich, W. E., Aciego, S. M., Depaolo, D. J. & Manga, M. Formation of box canyon, idaho, by megaflood: implications for seepage erosion on earth and mars. *Science* **320**, 1067–1070 (2008).
5. Lamb, M. P. & Fonstad, M. A. Rapid formation of a modern bedrock canyon by a single flood event. *Nat. Geosci.* **3**, 477–481 (2010).
6. Lamb, M. P., Mackey, B. H. & Farley, K. A. Amphitheater-headed canyons formed by megaflooding at Malad Gorge, Idaho. *Proc. Natl Acad. Sci. USA* **111**, 57–62 (2014).
7. Anton, L., Mather, A. E., Stokes, M., Muñoz-Martin, A. & de Vicente, G. Exceptional river gorge formation from unexceptional floods. *Nat. Commun.* **6**, 7963 (2015).
8. Baynes, E. R. C. et al. Erosion during extreme flood events dominates Holocene canyon evolution in northeast Iceland. *Proc. Natl Acad. Sci. USA* **112**, 2355–2360 (2015).
9. Kelsey, H. M. Formation of inner gorges. *CATENA* **15**, 433–458 (1988).
10. Densmore, A. L., Anderson, R. S., McAdoo, B. G. & Ellis, M. A. Hillslope evolution by bedrock landslides. *Science* **275**, 369–372 (1997).
11. Schlunegger, F. & Schneider, H. Relief-rejuvenation and topographic length scales in a fluvial drainage basin, napf area, central switzerland. *Geomorphology* **69**, 102–117 (2005).
12. Stock, J. D., Montgomery, D. R., Collins, B. D., Dietrich, W. E. & Sklar, L. Field measurements of incision rates following bedrock exposure: implications for process controls on the long profiles of valleys cut by rivers and debris flows. *Geological Society of America Bulletin* **117**, 174 (2005).
13. Dürst Stucki, M., Schlunegger, F., Christener, F., Otto, J.-C. & Götz, J. Deepening of inner gorges through subglacial meltwater—an example from the UNESCO entrench area, Switzerland. *Geomorphology* **139-140**, 506–517 (2012).
14. Beaud, F., Venditti, J. G., Flowers, G. E. & Koppes, M. Excavation of subglacial bedrock channels by seasonal meltwater flow. *Earth Surface Processes Landf.* **43**, 1960–1972 (2018).
15. Penck, W. Die morphologische Analyse: Ein Kapitel der physikalischen Geologie (J. Engelhorns Nachf., Stuttgart, 1924).
16. Koppes, M. N. & Hallet, B. Influence of rapid glacial retreat on the rate of erosion by tidewater glaciers. *Geology* **30**, 47 (2002).
17. Ballantyne, C. K. Paraglacial geomorphology. *Quat. Sci. Rev.* **21**, 1935–2017 (2002).
18. Meigs, A., Krugh, W. C., Davis, K. & Bank, G. Ultra-rapid landscape response and sediment yield following glacier retreat, Icy Bay, Southern Alaska. *Geomorphology* **78**, 207–221 (2006).
19. Penck, A. & Brückner, E. *Die Alpen im Eiszeitalter: Erster Band* (Chr. Herm. Tauchnitz, Leipzig, 1909).
20. McEwen, L. J., Matthews, J. A., Shakesby, R. A. & Berrisford, M. S. Holocene gorge excavation linked to boulder fan formation and frost weathering in a Norwegian alpine periglaciofluvial system. *Arct Antarct. Alp. Res.* **34**, 345–357 (2002).
21. Brocard, G. Y., van der Beek, P. A., Bourlès, D. L., Siame, L. L. & Mugnier, J.-L. Long-term fluvial incision rates and postglacial river relaxation time in the French western alps from 10be dating of alluvial terraces with assessment of inheritance, soil development and wind ablation effects. *Earth Planet. Sci. Lett.* **209**, 197–214 (2003).
22. Schlunegger, F. & Hinderer, M. Pleistocene/holocene climate change, re-establishment of fluvial drainage network and increase in relief in the swiss alps. *Terra Nova* **15**, 88–95 (2003).
23. Valla, P. G., van der Beek, P. A. & Lague, D. Fluvial incision into bedrock: Insights from morphometric analysis and numerical modeling of gorges incising glacial hanging valleys (western Alps, France). *J. Geophys. Res. Earth Surface* https://doi.org/10.1029/2008JF001079 (2010).
24. Cadisch, J. Zur talgeschichte von davos. *Jahresbericht der Naturforschenden Gesellschaft Graubünden* (1924).
25. Montgomery, D. R. & Korup, O. Preservation of inner gorges through repeated alpine glaciations. *Nat. Geosci.* **4**, 62–67 (2011).
26. Dixon, J. L. Deceptively old alpine gorges. *Nat. Geosci.* **4**, 8–9 (2011).
27. Hallet, B., Hunter, L. & Bogen, J. Rates of erosion and sediment evacuation by glaciers: a review of field data and their implications. *Glob. Planet. Change* **12**, 213–235 (1996).
28. Berger, C., McArdell, B. W. & Schlunegger, F. Direct measurement of channel erosion by debris flows, Illgraben, Switzerland. *J. Geophys. Res. Earth Surface* **116**, n/a–n/a (2011).
29. McCoy, S. W. et al. Sediment entrainment by debris flows: in situ measurements from the headwaters of a steep catchment. *J. Geophys. Res. Earth Surface* **117**, n/a–n/a (2012).
30. Bremer, M. & Sass, O. Combining airborne and terrestrial laser scanning for quantifying erosion and deposition by a debris flow event. *Geomorphology* **138**, 49–60 (2012).
31. Dietrich, A. & Krautblatter, M. Deciphering controls for debris–flow erosion derived from a lidar–recorded extreme event and a calibrated numerical model (Roßbichelbach, Germany). *Earth Surf. Process. Landf.* **44**, 1346–1361 (2019).
32. Reid, M. E. et al. Entrainment of bed sediment by debris flows: results from large-scale experiments. In *Proc. International Conference on Debris-Flow Hazards Mitigation: Mechanics, Prediction, and Assessment,* 367–374 (2011).
33. de Haas, T. & van Woerkom, T. Bed scour by debris flows: experimental investigation of effects of debris–flow composition. *Earth Surface Process. Landf.* **41**, 1951–1966 (2016).
34. Huang, M.-W., Pan, Y.-W. & Liao, J.-J. A case of rapid rock riverbed incision in a coseismic uplift reach and its implications. *Geomorphology* **184**, 98–110 (2013).
35. Cook, K. L., Turowski, J. M. & Hovius, N. River gorge eradication by downstream sweep erosion. *Nat. Geosci.* **7**, 682–686 (2014).
36. Beer, A. R., Turowski, J. M. & Kirchner, J. W. Spatial patterns of erosion in a bedrock gorge. *J. Geophys. Res. Earth Surface* **122**, 191–214 (2017).
37. Takahashi, T. *Debris Flow: Mechanics, Prediction and Countermeasures* (Taylor & Francis Group, London, UK, 2007).
38. Hungr, O., McDougall, S. & Bovis, M. J. Entrainment of material by debris flows. In Jakob, M. & Hungr, O. (eds.) *Debris-Flow Hazards and Related Phenomena*, 135–155 (Springer, Berlin, 2005).
39. Stock, J. D. & Dietrich, W. E. Erosion of steep land valleys by debris flows. *Geol. Soc. Am. Bull.* **118**, 1125–1148 (2006).
40. Scott, D. N. & Wohl, E. E. Bedrock fracture influences on geomorphic process and form across process domains and scales. *Earth Surface Process. Landf.* **44**, 27–45 (2019).
41. Marcotte, A. L., Neudorf, C. M. & Langston, A. L. Lateral bedrock erosion and valley formation in a heterogeneously layered landscape, northeast Kansas. *Earth Surf. Process. Landf.* **46**, 2248–2263 (2021).

42. Foley, M. G. Bed-rock incision by streams. *GSA Bull.* **91**, 2189–2213 (1980).

43. Wohl, E. E., Greenbaum, N., Schick, A. P. & Baker, V. R. Controls on bedrock channel incision along Nahal Paran, Israel. *Earth Surface Process. Landf.* **19**, 1–13 (1994).

44. Baker, V. R. & Kale, V. S. The role of extreme floods in shaping bedrock channels. In Tinkler, J. & Wohl, E. (eds.) *Rivers Over Rock: Fluvial Processes in Bedrock Channels*, vol. 107 of *Geophysical Monograph Series*, 153–165 (American Geophysical Union, Washington, D. C., 1998).

45. Hancock, G. S., Anderson, R. S. & Whipple, K. X. Beyond power: Bedrock river incision process and form. In Tinkler, J. & Wohl, E. (eds.) *Rivers Over Rock: Fluvial Processes in Bedrock Channels*, Geophysical Monograph Series, 35–60 (American Geophysical Union, Washington, D. C., 1998).

46. Sklar, L. & Dietrich, W. E. River longitudinal profiles and bedrock incision models: Stream power and the influence of sediment supply. In Tinkler, J. & Wohl, E. (eds.) *Rivers Over Rock: Fluvial Processes in Bedrock Channels*, vol. 107 of *Geophysical Monograph Series*, 237–260 (American Geophysical Union, Washington, D. C., 1998).

47. Whipple, K. X., Snyder, N. P. & Dollenmayer, K. Rates and processes of bedrock incision by the upper Ukak river since the 1912 Novarupta ash flow in the valley of ten thousand smokes, alaska. *Geology* **28**, 835–838 (2000).

48. Sklar, L. S. & Dietrich, W. E. Sediment and rock strength controls on river incision into bedrock. *Geology* **29**, 1087 (2001).

49. Iverson, R. M. The debris-flow rheology myth. In Rickenmann, D. & Chen, C. L. (eds.) *Debris-Flow Hazards Mitigation: Mechanics, Prediction, and Assessment*, 303–314 (Millpress, Rotterdam, 2003).

50. Sklar, L. S. & Dietrich, W. E. A mechanistic model for river incision into bedrock by saltating bed load. *Water Resour. Res.* https://doi.org/10.1029/2003WR002496 (2004).

51. Whipple, K. X. Bedrock rivers and the geomorphology of active orogens. *Annu. Rev. Earth Planet. Sci.* **32**, 151–185 (2004).

52. Turowski, J. M., Hovius, N., Meng-Long, H., Lague, D. & Men-Chiang, C. Distribution of erosion across bedrock channels. *Earth Surface Process. Landf.* **33**, 353–363 (2008).

53. Turowski, J. M., Badoux, A., Leuzinger, J. & Hegglin, R. Large floods, alluvial overprint, and bedrock erosion. *Earth Surface Process. Landf.* **38**, 947–958 (2013).

54. Whipple, K. X., DiBiase, R. A. & Crosby, B. T. Bedrock rivers. In Shroder, J. F. (ed.) *Treatise on Geomorphology*, 550–573 (Academic Press, San Diego, 2013).

55. Cook, K. L., Turowski, J. M. & Hovius, N. A demonstration of the importance of bedload transport for fluvial bedrock erosion and knickpoint propagation. *Earth Surface Process Landf.* **38**, 683–695 (2013).

56. Beer, A. R. & Turowski, J. M. Bedload transport controls bedrock erosion under sediment-starved conditions. *Earth Surf. Dyn.* **3**, 291–309 (2015).

57. Chatanantavet, P. & Parker, G. Experimental study of bedrock channel alluviation under varied sediment supply and hydraulic conditions. *Water Resour. Res.* https://doi.org/10.1029/2007WR006581 (2008).

58. Mishra, J. & Inoue, T. Alluvial cover on bedrock channels: applicability of existing models. *Earth Surf. Dyn.* **8**, 695–716 (2020).

59. Mishra, J., Inoue, T., Shimizu, Y., Sumner, T. & Nelson, J. M. Consequences of abrading bed load on vertical and lateral bedrock erosion in a curved experimental channel. *Journal of Geophys. Res. Earth Surf.* **123**, 3147–3161 (2018).

60. Smart, C. C. A Statistical Analysis of Cave Meanders. M.sc. thesis, University of Alberta, Edmonton, Alberta, Canada (1977).

61. Stark, C. P. et al. The climatic signature of incised river meanders. *Science* **327**, 1497–1501 (2010).

62. Barbour, J. R. et al. Magnitude-frequency distributions of boundary shear stress along a rapidly eroding bedrock river. *Geophys. Res. Lett.* https://doi.org/10.1029/2008GL035786 (2009).

63. Janes, V. J. J., Nicholas, A. P., Collins, A. L. & Quine, T. A. Analysis of fundamental physical factors influencing channel bank erosion: results for contrasting catchments in England and Wales. *Environ. Earth Sci.* **76**, 307 (2017).

64. Micheli, E. R. & Kirchner, J. W. Effects of wet meadow riparian vegetation on streambank erosion. 1. remote sensing measurements of streambank migration and erodibility. *Earth Surf. Process. Landf.* **27**, 627–639 (2002).

65. Laubel, A., Kronvang, B., Hald, A. B. & Jensen, C. Hydromorphological and biological factors influencing sediment and phosphorus loss via bank erosion in small lowland rural streams in denmark. *Hydrol. Process.* **17**, 3443–3463 (2003).

66. Ikeda, S., Parker, G. & Sawai, K. Bend theory of river meanders. part 1. Linear development. *J. Fluid Mech.* **112**, 363 (1981).

67. Hickin, E. J. & Nanson, G. C. Lateral migration rates of river bends. *J. Hydraulic Eng.* **110**, 1557–1567 (1984).

68. Thorne, C. R. Bank erosion and meander migration of the Red and Mississippi river, USA. Hydrology for the Water Management of Large River Basins. In *Proceedings of the Vienna Symposium* 301–313 (IAHS, 1991).

69. Langbein, W. B. & Leopold, L. B. in *Rivers Rivers and River Terraces. Geographical Readings*. (eds Dury, G. H.) 238–263 (Springer, 1996).

70. Hooke, J. Coarse sediment connectivity in river channel systems: a conceptual framework and methodology. *Geomorphology* **56**, 79–94 (2003).

71. Julien, P. Y. (ed.) *River Mechanics* (Cambridge University Press, 2012).

72. Hey, R. D. & Thorne, C. R. Secondary flows in river channels. *Area* **7**, 191–195 (1975).

73. Wohl, E. & Ikeda, H. Experimental simulation of channel incision into a cohesive substrate at varying gradients. *Geology* **25**, 295 (1997).

74. Johnson, J. P. & Whipple, K. X. Feedbacks between erosion and sediment transport in experimental bedrock channels. *Earth Surf. Process. Landf.* **32**, 1048–1062 (2007).

75. Whipple, K. X. & Tucker, G. E. Dynamics of the stream-power river incision model: Implications for height limits of mountain ranges, landscape response timescales, and research needs. *J. Geophys. Res.* **104**, 17661–17674 (1999).

76. Seidl, M. A. & Dietrich, W. E. The problem of channel erosion into bedrock. In Schmidt, K.-H. (ed.) *Functional Geomorphology*, Catena Supplement, 101–124 (Catena-Verl., Cremlingen-Destedt, 1992).

77. Finnegan, N. J., Roe, G., Montgomery, D. R. & Hallet, B. Controls on the channel width of rivers: Implications for modeling fluvial incision of bedrock. *Geology* **33**, 229 (2005).

78. Korup, O. & Schlunegger, F. Bedrock landsliding, river incision, and transience of geomorphic hillslope-channel coupling: Evidence from inner gorges in the Swiss Alps. *J. Geophys. Res.* https://doi.org/10.1029/2006JF000710 (2007).

79. Valla, P. G., van der Beek, P. A. & Carcaillet, J. Dating bedrock gorge incision in the French western alps (ecrins-pelvoux massif) using cosmogenic 10 be. *Terra Nova* **22**, 18–25 (2010).

80. Lague, D. The stream power river incision model: evidence, theory and beyond. *Earth Surf. Process. Landf.* **39**, 38–61 (2014).

81. Howard, A. D. & Kerby, G. Channel changes in badlands. *Geol. Soc. Am. Bull.* **94**, 739 (1983).

82. Howard, A. D., Dietrich, W. E. & Seidl, M. A. Modeling fluvial erosion on regional to continental scales. *J. Geophys. Res.* **99**, 13971–13986 (1994).

83. Montgomery, D. R. & Foufoula-Georgiou, E. Channel network source representation using digital elevation models. *Water Resour. Res.* **29**, 3925–3934 (1993).

84. Howard, A. D. Long profile development of bedrock channels: Interaction of weathering, mass wasting, bed erosion, and sediment transport. In Tinkler, J. & Wohl, E. (eds.) *Rivers Over Rock: Fluvial Processes in Bedrock Channels*, vol. 107 of *Geophysical Monograph Series*, 297–319 (American Geophysical Union, Washington, D. C., 1998).

85. Snyder, N. P., Whipple, K. X., Tucker, G. E. & Merritts, D. J. Landscape response to tectonic forcing: Digital elevation model analysis of stream profiles in the mendocino triple junction region, northern california. *Geol. Soc. Am. Bull.* **112**, 1250–1263 (2000).

86. Stock, J. & Dietrich, W. E. Valley incision by debris flows: evidence of a topographic signature. *Water Resour. Res.* https://doi.org/10.1029/2001WR001057 (2003).

87. Pierson, T. C. Hyperconcentrated flow—transitional process between water flow and debris flow. In Jakob, M. & Hungr, O. (eds.) *Debris-Flow Hazards and Related Phenomena*, 159–202 (Springer, Berlin, 2005).

88. Lai, L. S.-H., Roering, J. J., Finnegan, N. J., Dorsey, R. J. & Yen, J.-Y. Coarse sediment supply sets the slope of bedrock channels in rapidly uplifting terrain: field and topographic evidence from eastern taiwan. *Earth Surf. Process. Landf.* **46**, 2671–2689 (2021).

89. Lamb, M. P., Dietrich, W. E. & Sklar, L. S. A model for fluvial bedrock incision by impacting suspended and bed load sediment. *J. Geophys. Res.* https://doi.org/10.1029/2007JF000915 (2008).

90. Li, T., Venditti, J. G., Sklar, L. S. & Lamb, M. P. Lateral erosion of bedrock channel banks by bedload and suspended load. *J. Geophys. Res. Earth Surf.* **128** e2022JF006806 (2023).

91. Scheingross, J. S., Brun, F., Lo, D. Y., Omerdin, K. & Lamb, M. P. Experimental evidence for fluvial bedrock incision by suspended and bedload sediment. *Geology* **42**, 523–526 (2014).

92. Costa, J. E. & O'Connor, J. E. Geomorphically effective floods. In Costa, J. E., Miller, A. J., Potter, K. W. & Wilcock, P. R. (eds.) *Natural and Anthropogenic Influences in Fluvial Geomorphology*, vol. 89, 45–56 (American Geophysical Union, Washington, D.C., 1995).

93. Johnson, J. P. L., Whipple, K. X., Sklar, L. S. & Hanks, T. C. Transport slopes, sediment cover, and bedrock channel incision in the Henry Mountains, Utah. *J. Geophys. Res. Earth Surf.* https://doi.org/10.1029/2007JF000862 (2009).

94. DiBiase, R. A., Whipple, K. X., Heimsath, A. M. & Ouimet, W. B. Landscape form and millennial erosion rates in the San Gabriel mountains, ca. *Earth Planet Sci. Lett.* **289**, 134–144 (2010).

95. Reis, O. Erläuterungen zur geologischen karte des wettersteingebirges. *Geogn. Jahresh.* **23**, 61–104 (1910).

96. Miller, H. *Zur Geologie des westlichen Wetterstein- und Mieminger Gebirges (Tirol): Strukturzusammenhänge am Ostrand des Ehrwalder Beckens*. Dissertation, Ludwig-Maximilians-Universität, München (1962).

97. Hornung, T. & Haas, U. Erläuterungen zur Geologischen Karte 1:25000, 8531/8631 Zugspitze. 8532/8632 Garmisch-Partenkirchen. 151 (Bavarian Environmental Agency, 2017).

98. Rappl, A., Wetzel, K. F., Büttner, G. & Scholz, M. Tracerhydrologische untersuchungen am partnachursprung. *Hydrol. Wasserbewirtsch.* **54**, 222–230 (2010).

99. Mamot, P., Weber, S., Eppinger, S. & Krautblatter, M. A temperature-dependent mechanical model to assess the stability of degrading permafrost rock slopes. *Earth Surface Dyn.* **9**, 1125–1151 (2021).

100. Pierson, T. C. Distinguishing between debris flows and floods from field evidence in small watersheds: USGS fact sheet 2004-3142 (2005).

101. Lague, D., Brodu, N. & Leroux, J. Accurate 3d comparison of complex topography with terrestrial laser scanner: Application to the rangitikei canyon (n-z). *ISPRS J. Photogramm. Remote Sens.* **82**, 10–26 (2013).

102. Clauset, A., Shalizi, C. R. & Newman, M. E. J. Power-law distributions in empirical data. *SIAM Rev.* **51**, 661–703 (2009).

103. Rosser, N. J., Petley, D. N., Lim, M., Dunning, S. A. & Allison, R. J. Terrestrial laser scanning for monitoring the process of hard rock coastal cliff erosion. *Q. J. Eng. Geol. Hydrogeol.* **38**, 363–375 (2005).

104. Hartshorn, K., Hovius, N., Dade, W. B. & Slingerland, R. L. Climate-driven bedrock incision in an active mountain belt. *Science* **297**, 2036–2038 (2002).

105. Bennett, G. L., Molnar, P., Eisenbeiss, H. & McArdell, B. W. Erosional power in the Swiss Alps: characterization of slope failure in the Illgraben. *Earth Surf. Process. Landf.* **37**, 1627–1640 (2012).

106. Hovius, N., Stark, C. P. & Allen, P. A. Sediment flux from a mountain belt derived by landslide mapping. *Geology* **25**, 231 (1997).

107. Guzzetti, F., Malamud, B. D., Turcotte, D. L. & Reichenbach, P. Power-law correlations of landslide areas in central italy. *Earth Planet. Sci. Lett.* **195**, 169–183 (2002).

108. Dussauge-Peisser, C. et al. Probabilistic approach to rock fall hazard assessment: potential of historical data analysis. *Nat. Hazards Earth Syst. Sci.* **2**, 15–26 (2002).

109. Malamud, B. D., Turcotte, D. L., Guzzetti, F. & Reichenbach, P. Landslide inventories and their statistical properties. *Earth Surf. Process. Landf.* **29**, 687–711 (2004).

110. Johnson, J. P. L., Whipple, K. X. & Sklar, L. S. Contrasting bedrock incision rates from snowmelt and flash floods in the Henry mountains, Utah. *Geol. Soc. Am. Bull.* **122**, 1600–1615 (2010).

111. Tinkler, J. & Wohl, E. A primer on bedrock channels. In Tinkler, J. & Wohl, E. (eds.) *Rivers Over Rock: Fluvial Processes in Bedrock Channels*, Geophysical Monograph Series (American Geophysical Union, Washington, D. C., 1998).

112. Garvin, C. D., Hanks, T. C., Finkel, R. C. & Heimsath, A. M. Episodic incision of the Colorado River in Glen Canyon, Utah. *Earth Surf. Process. Landf.* **30**, 973–984 (2005).

113. Saillard, M. et al. Late quaternary incision rates in the vésubie catchment area (southern French alps) from in situ-produced 36 cl cosmogenic nuclide dating: tectonic and climatic implications. *J. Geophys. Res. Earth Surf.* **119**, 1121–1135 (2014).

114. Schaller, M. et al. Fluvial bedrock incision in the active mountain belt of Taiwan from in situ-produced cosmogenic nuclides. *Earth Surf. Process. Landf.* **30**, 955–971 (2005).

115. Burbank, D. W. et al. Bedrock incision, rock uplift and threshold hillslopes in the northwestern Himalayas. *Nature* **379**, 505–510 (1996).

116. Richardson, K. & Carling, P. *A Typology of Sculpted Forms in Open Bedrock Channels*, vol. 392 of *Special paper* (Geological Society of America, Boulder Colo. USA, 2005).

117. Whipple, K. X., Hancock, G. S. & Anderson, R. S. River incision into bedrock: Mechanics and relative efficacy of plucking, abrasion, and cavitation. *Geol. Soc. Am. Bull.* **112**, 490–503 (2000).

118. Whipple, K. X. & Tucker, G. E. Implications of sediment-flux-dependent river incision models for landscape evolution. *J. Geophys. Res.* **107** (2002).

119. Hsu, L., Dietrich, W. E. & Sklar, L. S. Experimental study of bedrock erosion by granular flows. *J. Geophys. Res.* **113** (2008).

120. Iverson, R. M. The physics of debris flows. *Rev. Geophys.* **35**, 245–296 (1997).

121. Chatanantavet, P. & Parker, G. Physically based modeling of bedrock incision by abrasion, plucking, and macroabrasion. *J. Geophys. Res.* https://doi.org/10.1029/2008JF001044 (2009).

122. Rieke-Zapp, D. H., Beer, A., Turowski, J. M. & Campana, L. In situ measurement of bedrock erosion. *ISPRS - International Archives of the Photogrammetry, Remote Sensing and Spatial Information Sciences* **XXXIX-B5**, 429–433 (2012).

123. Wohl, E. Bedrock channel morphology in relation to erosional process. In Tinkler, J. & Wohl, E. (eds.) *Rivers Over Rock: Fluvial Processes in Bedrock Channels*, vol. 107 of *Geophysical Monograph Series*, 133–152 (American Geophysical Union, Washington, D.C., 1998).

124. Ouimet, W. B., Whipple, K. X., Crosby, B. T., Johnson, J. P. & Schildgen, T. F. Epigenetic gorges in fluvial landscapes. *Earth Surf. Process. Landf.* **33**, 1993–2009 (2008).

125. Finnegan, N. J., Schumer, R. & Finnegan, S. A signature of transience in bedrock river incision rates over timescales of 10(4)-10(7) years. *Nature* **505**, 391–394 (2014).

126. Hirtlreiter, G. *Spät- und postglaziale Gletscherschwankungen im Wettersteingebirge und seiner Umgebung*. Dissertation, Ludwig-Maximilians-Universität **15**, 154 (1992).

127. Steinemann, O. et al. Glacial erosion by the Trift glacier (Switzerland): Deciphering the development of riegels, rock basins and gorges. *Geomorphology* **375**, 107533 (2021).

128. Jansen, J. D. et al. Inner gorges cut by subglacial meltwater during fennoscandian ice sheet decay. *Nat. Commun.* **5**, 3815 (2014).

129. Besl, P. J. & McKay, N. D. A method for registration of 3-D shapes. *IEEE Trans. Pattern Anal. Mach. Intellig.* **14**, 239–256 (1992).

130. Chen, Y. & Medioni, G. Object modeling by registration of multiple range images. *Image Vision Comput.* **10**, 145–155 (1992).

131. Zhang, Z. Iterative point matching for registration of free-form curves and surfaces. *Int. J. Comput. Vision* **13**, 119–152 (1994).

132. Abellán, A., Calvet, J., Vilaplana, J. M. & Blanchard, J. Detection and spatial prediction of rockfalls by means of terrestrial laser scanner monitoring. *Geomorphology* **119**, 162–171 (2010).

133. Abellán, A., Vilaplana, J. M., Calvet, J., García-Sellés, D. & Asensio, E. Rockfall monitoring by terrestrial laser scanning—case study of the basaltic rock face at castellfollit de la roca (Catalonia, Spain). *Nat. Hazards arth Syst. Sci.* **11**, 829–841 (2011).

134. Williams, J. G., Rosser, N. J., Hardy, R. J., Brain, M. J. & Afana, A. A. Optimising 4-d surface change detection: an approach for capturing rockfall magnitude–frequency. *Earth Surf. Dyn.* **6**, 101–119 (2018).

135. Rosser, N., Lim, M., Petley, D., Dunning, S. & Allison, R. Patterns of precursory rockfall prior to slope failure. *J. Geophys. Res.* **112** (2007).

136. Blasone, G., Cavalli, M., Marchi, L. & Cazorzi, F. Monitoring sediment source areas in a debris-flow catchment using terrestrial laser scanning. *CATENA* **123**, 23–36 (2014).

137. Teza, G., Galgaro, A., Zaltron, N. & Genevois, R. Terrestrial laser scanner to detect landslide displacement fields: a new approach. *Int. J. Remote Sens.* **28**, 3425–3446 (2007).

138. Monserrat, O. & Crosetto, M. Deformation measurement using terrestrial laser scanning data and least squares 3d surface matching. *ISPRS J. Photogramm. Remote Sens.* **63**, 142–154 (2008).

139. Hodge, R. A. Using simulated terrestrial laser scanning to analyse errors in high-resolution scan data of irregular surfaces. *ISPRS J. Photogramm. Remote Sens.* **65**, 227–240 (2010).

140. Soudarissanane, S., Lindenbergh, R., Menenti, M. & Teunissen, P. Scanning geometry: influencing factor on the quality of terrestrial laser scanning points. *ISPRS Journal of Photogrammetry and Remote Sensing* **66**, 389–399 (2011).

141. Draebing, D., Mayer, T., Jacobs, B. & McColl, S. T. Alpine Rockwall erosion patterns follow elevation-dependent climate trajectories. *Commun. Earth Environ.* **3** (2022).

142. Dai, F. & Lee, C. Frequency–volume relation and prediction of rainfall-induced landslides. *Eng. Geol.* **59**, 253–266 (2001).

143. Dussauge, C., Grasso, J.-R. & Helmstetter, A. Statistical analysis of rockfall volume distributions: Implications for rockfall dynamics. *J. Geophys. Res.: Solid Earth* **108** (2003).

144. Hergarten, S. Landslides, sandpiles, and self-organized criticality. *Nat. Hazards Earth Syst. Sci.* **3**, 505–514 (2003).

145. Barlow, J. et al. Modeling cliff erosion using negative power law scaling of rockfalls. *Geomorphology* **139-140**, 416–424 (2012).

146. Strunden, J., Ehlers, T. A., Brehm, D. & Nettesheim, M. Spatial and temporal variations in rockfall determined from ITS measurements in a deglaciated valley, Switzerland. *J. Geophys. Res. Earth Surf.* **120**, 1251–1273 (2015).

147. Hartmeyer, I. et al. A 6-year lidar survey reveals enhanced rockwall retreat and modified rockfall magnitudes/frequencies in deglaciating cirques. *Earth Surf. Dyn.* **8**, 753–768 (2020).

148. Brardinoni, F. & Church, M. Representing the landslide magnitude–frequency relation: Capilano river basin, British Columbia. *Earth Surf. Process. Landf.* **29**, 115–124 (2004).

149. Silverman, B. W. Using kernel density estimates to investigate multimodality. *J. R. Stat. Soc. Ser. B (Methodol.)* **43**, 97–99 (1981).

Author contributions
All authors contributed to the work presented in this paper. V.S. and B.J. collected the data and performed the initial analysis. V.S. performed the extensive analysis with helpful contributions and error identifications by B.J.; V.S. designed and wrote the paper; V.S. and M.K. interpreted the results and added finishing touches to the paper.

Competing interests
The authors declare no competing interests.

Additional information
Supplementary information The online version contains supplementary material available at https://doi.org/10.1038/s43247-024-01353-3.

Correspondence and requests for materials should be addressed to Verena Stammberger.

Peer review information *Communications Earth & Environment* thanks Larry Syu-Heng Lai and the other, anonymous, reviewer(s) for their contribution to the peer review of this work. Primary Handling Editors: Adam Switzer, Joe Aslin, Heike Langenberg. A peer review file is available.

Reprints and permissions information is available at http://www.nature.com/reprints

Publisher's note Springer Nature remains neutral with regard to jurisdictional claims in published maps and institutional affiliations.